Supporting Information

Macfarlane et al. 10.1073/pnas.1416489111

SI Text

SI Materials and Methods. All gold nanoparticles were obtained from BB International and all oligonucleotides were obtained from Integrated DNA Technologies or synthesized using a Bioautomation Mermade 48 DNA synthesizer. Synthesized oligonucleotides were purified with reverse-phase high performance liquid chromatography on a Varian Microsorb C18 column (10 μm, 300 × 10 mm) and fractions were collected in polypropylene conical tubes. DNA functionalization was conducted in accordance with literature procedures (1, 2). Oligonucleotides with a 3′-propyldisulfide (Glen Research) were reduced by treating them in an aqueous solution of 100 mM DTT (Sigma-Aldrich) for approximately 1 h, then subsequently purified using size-exclusion chromatography with a Sephadex G-25 column (NAP5, GE Healthcare) to remove excess DTT, and the desired eluate was collected in 1.5 mL Eppendorf centrifuge tubes. The oligonucleotides were then added to colloidal solutions of gold nanoparticles (3 nmol DNA per ml AuNPs) and allowed to incubate overnight. The solutions were then slowly salted via stepwise additions of 1% SDS, 1.0 M sodium phosphate (pH = 7.4), and aliquots of 2.0 M NaCl, followed by 10 s of sonication. Once final buffer concentrations of 0.5 M NaCl, 10 mM $NaPO_4$, and 0.01% SDS were reached, the solution was allowed to sit for 16 h to maximize DNA loading. Excess DNA strands were removed by centrifugation (~21,000 relative centrifugal force for 60 min), followed by removal of the supernatant and redispersal of the pellet in 0.02% SDS. After three rounds of centrifugation and removal of the supernatant, the pellet was redispersed in 0.5 M PBS. The extinction coefficient used for calculating 10-nm particle concentrations was 9.55×10^7 M^{-1} cm^{-1}.

Assembly of Face-Centered Cubic Superlattices. Samples were prepared in a 0.5-mL Eppendorf centrifuge tube by combining the AuNPs coated with thiolated DNA and its complementary linker sequence that also contained a 3′ self-complementary "sticky end," and allowing the resulting mixture to sit at room temperature for ~30 min (some of the strongest sticky ends required brief annealing at ~45 °C to induce aggregation). Buffer solutions were then added to the aggregated nanoparticles to bring the samples to the appropriate salt concentration (as outlined in the main text), and final AuNP concentrations of 50 nM. The samples used for kinetics experiments were then held at either room temperature or ~4 °C to prevent reorganization, and the samples that were annealed outside of the path of the X-ray beam were placed at temperatures ~1 °C below their melting temperature (controlled to within 0.1 °C) for periods ranging from several hours to overnight. The samples were then transferred to 1.5-mm quartz capillary tubes (Charles Supper Company) for SAXS measurements.

Small-Angle X-Ray Scattering. Small-angle X-ray scattering (SAXS) experiments were performed at the DuPont–Northwestern–Dow Collaborative Access Team beamline of Argonne National Laboratory's Advanced Photon Source with X-rays of 1.24-Å wavelength (10 keV), calibrated using silver behenate as a standard. Two sets of slits were used to define and collimate the X-ray beam, and a pinhole was used to remove parasitic scattering. The X-ray beam cross-section was ~1.0×1.0 mm^2 in dimension and exposure times varied from 0.1 to 0.5 s. Exposure times greater than 1 s were observed to damage the sample, so the sample stage was moved in between exposures during the kinetics experiments to prevent sample degradation. Scattered radiation was detected using a CCD area detector and azimuthally averaging of the 2D scattering data were used to obtain one-dimensional SAXS data. Profiles of scattering intensity were then generated as a function of scattering vector q:

$$q = 4\pi \sin(\theta)/\lambda,$$

where θ is half of the scattering angle, 2θ, and λ is the wavelength of the X-ray radiation. Dark current frames were subtracted from all data; scattering from buffer and DNA were negligible compared with that due to the nanoparticle superlattices.

A stage with thermal control was used to closely monitor the temperature of each sample during the kinetics experiments. To maintain consistency for a single sample measured at different temperatures, large batches of aggregates were prepared for each sample type and separated into multiple aliquots. At the beginning of each experiment, the temperature was set to 22 °C (or 4 °C if the sample was found to form crystals at ambient temperature) and an initial scan of the disordered aggregate was taken. The temperature was then quickly raised to a temperature slightly above, below, or at the sample's melting temperature. A scan was immediately taken once that temperature was reached and subsequent scans were taken as quickly as possible for the first few minutes of annealing. After this initial period, the rate at which scans were taken was slowly reduced as the differences in the scattering patterns became less pronounced. The endpoint of each run was reached once consecutive scans displayed indistinguishable scattering patterns, or the samples showed signs of X-ray beam damage. The time of each kinetics experiment varied from ~5 to 30 min, depending on both the nature of the sample as well as temperature being probed.

The time that each system required to achieve reorganization was tabulated by determining the time point in which there was a transition from a disordered to an ordered state. The transition points were chosen as the data scans in which a local minima was observed in between the third- and fourth-order fcc scattering peaks (Fig. S1). Although the disordered to fcc transition is a slow and gradual process and the transition point is essentially an arbitrarily chosen value, all comparisons made in this work are qualitative and the same basic peak shapes (and peak shape changes) were observed for all systems, indicating that this easily observable time point allows for unambiguous comparisons between systems with widely varied kinetics of reorganization. The error for these time points was calculated as half of the average time between the transition point and the data points immediately preceding and following it. This provides a reasonable approximation for error based on both the instrument and user by setting the lower error bound as the halfway point between the preceding scan and transition point scan, and the upper bound as the halfway point between the transition point scan and subsequent scan.

Mathematically more rigorous comparisons were also attempted using batch-processed peak-fitting analyses to more clearly understand the reorganization process (*vide infra*); however, several factors resulted in significant variation in the quality and reliability of the peak fitting to the experimental data, rendering these methods infeasible for direct comparisons. Specifically, the gradual change from a disordered to ordered state, the fact that the third- and fourth-order fcc peaks overlap with peaks in the initial disordered scattering pattern, X-ray beam damage leading to decreased peak intensity, significant form factor baseline arising from the gold nanoparticles, short X-ray exposure times (necessary to prevent significant beam damage during experiments) leading to reduced signal-to-noise values, and the large

data sets used to examine the reorganization process made the determination of a transition point that is clearly and unequivocally comparable between all data sets challenging. Within a data set, qualitative comparisons could often be made (Tables S3–S5), but the arbitrary choice of an easily observable peak shape (the local minima between the third- and fourth-order peaks) provided much more reliable and straightforward comparison of all of the data in this work.

Melting Transition Determination with UV-Vis Spectroscopy. The melting temperature of each sample was determined using an Agilent Cary 5000 UV-Vis–near-infrared spectrophotometer. An aliquot of a disordered aggregate for each system was diluted in buffer of the appropriate salt concentration such that the overall absorbance at 520 nm was between 0.1 and 1.0 (~2 nM with respect to the nanoparticles; concentrations matching those used in the SAXS experiments could not be used as those gave absorbance values outside of the Beer–Lambert range), and placing the mixture in a cuvette equipped with a magnetic stir bar. The cuvettes were then placed in a multicell holder with thermal control and sample absorbance was monitored at 260 and 520 nm while the thermal stage was heated at a rate of 0.25 °C/min. The melting temperature of each system was determined as the largest value in the first derivate of the melting curve. It is important to note that although this procedure was followed for all samples, slight variations (±1–3 °C) in melting temperature were observed for a sample with the same identity (i.e., sticky end sequence, number of linker equivalents, and/or salt concentration) but prepared at different times; this is most likely due to deviations in aggregate size (3). Therefore, all reported melting temperatures represent an average temperature when multiple melting experiments were performed for a given sample type.

Domain Size Calculations and Crystal Quality Comparisons. Average crystalline domain sizes were calculated using the Scherrer formula:

$$t = \frac{0.9\lambda}{B\cos\theta},$$

where t is the diameter of the crystalline domain in angstroms (assuming a pseudospherical crystal domain shape), λ is the wavelength of scattered X-rays in angstroms, θ is the diffraction angle associated with the q_0 peak, and B is the angular full width at half maximum of the q_0 peak (4).

It is important to note that the aggregates observed in solution were macroscopic in size (up to several millimeters in diameter), and readily observable with the naked eye. The crystal domain sizes presented herein are the diameters of the domains in which the nanoparticles can be defined by a single crystallographic lattice. In other words, the assembly process does not produce discrete colloidal crystals existing in solution, but rather continuous macroscopic aggregates wherein the nanoparticles in any crystalline domain within the aggregate are ordered relative to each other.

Data Analysis. Scattering data were analyzed by nonlinear least squares fitting implemented in MATLAB (The MathWorks, Inc.) using a script designed to consistently obtain parameters for all SAXS data. The results of one such fitting is shown in Fig. S4 as an example. First, the scattering intensity was divided by the form factor to obtain the structure factor. Our analysis focused on the region from 0.02 to 0.07 $Å^{-1}$, which corresponds to the first four peaks of an fcc lattice for these particles (black dots in Fig. S4). To estimate the background from which the peaks extend, the lowest three points from each valley region (~0.02, ~0.04, and ~0.07 $Å^{-1}$) were used to fit the background to a cubic function (orange line in Fig. S4). Next, the structure factor with the cubic background subtracted was fit in the region around the first peak to a Lorentzian to obtain estimates for the peak height, location, and width. These values were used as seed values for fitting the first peak region of the original structure factor to a 10-parameter fit that included a cubic background, a skewed Lorentzian (5), and a Lorentzian that is located at $(4/3)^{1/2}$ times the position of the first peak to encompass the second peak (light blue curve in Fig. S4). We found that, for fcc crystals of this type, it was not possible to fit the first two peaks independently and so including both peaks in this fit allowed for a more accurate determination of the shape of the first peak. Using a skewed Lorentzian for the first peak was found to be necessary to account for the imperfect background subtraction. The magnitude, location, width, and skewness of the first peak with associated uncertainty from fitting were saved for further analysis. Next, the third and fourth peaks were fit using a 10-parameter fit to the sum of two Lorentzians over a cubic background (light green curve in Fig. S4). The magnitudes, locations, and width of each of these peaks with associated fitting uncertainty were saved for further analysis.

In addition to this analysis, a much simpler calculation was done to estimate the width of the first peak. First, the valley region on either side of the first peak was used to fit a quadratic function to estimate the background of the first peak. Next, the maximum value of the first peak over the quadratic background is identified and used as a simple estimate of the peak height (vertical red line in Fig. S4). Finally, the half-max point on each side of the first peak is identified as the location where the structure factor is closest to half the value of the peak height above the background; this position is used to compute the half-width at half-max from each side of the curve (horizontal red lines in Fig. S4).

Analysis of the fitted data for each kinetics experiment was carried out by plotting the position or FWHM of a given scattering peak versus the time of each respective scan (where the initial disordered scan is set as time equals 0). This produces a curve with an exponential decay as the sample transitions from a disordered to ordered arrangement. Upon fitting this data with an exponential function [$y = A_1{*}\exp(-x/t_1) + y_0$, where y is the position or FWHM of the scattering peak in $Å^{-1}$ and x is the corresponding time for that scan in seconds], the decay time constant (t_1) and asymptote (y_0) values for each temperature tested were tabulated. The decay time constant reflects the relative speed at which a sample reorganizes into a lattice, with larger time constants correlating to slower reorganization rates, and the asymptote signifies the minimum peak breadth (and thus maximum crystal quality) achieved for a given sample during a kinetics experiment.

From this data, a general trend can be observed: low annealing temperatures lead to slow reorganization kinetics and broad asymptote peak widths; in contrast, high temperatures induce fast reorganization, which end with narrow peaks. However, it should be noted that this trend does not always hold and, in several instances, the highest temperatures tested for a given system yielded slower time constants than experiments performed at lower temperatures. In addition to multiple factors discussed in the previous section that resulted in inconsistencies between samples during the peak fitting, aggregate melting was frequently observed at the late time points of in situ experiments that were performed at high temperatures. As such, scattering data collected after the onset of melting contained broadened peaks as the structure factor was gradually lost while the lattice was melting apart. Therefore, the last scans of a given kinetics experiment at these high temperatures were not able to accurately depict the final crystal quality and caused the fittings to give time constants with significant degrees of error.

Thermodynamic Model of Programmable Atom Equivalent (PAE) Reorganization. To gain insight into the reorganization process, we constructed a thermodynamic model that incorporates polyvalent effects. This model is based on the assumption that aggregation is a two-step process, first two free particles bind via a single DNA linkage and then a second DNA linkage is formed. The central hypothesis of this model is that for reorganization to

occur there must be a population of the singly bound intermediate, so it may be possible to predict the reorganization kinetics through the population of the singly bound intermediate. The model is defined by the following chemical reactions,

$$A + A \underset{k_{off}}{\overset{k_{on}}{\rightleftarrows}} AA \qquad \textbf{[S1]}$$

$$AA \underset{k_r}{\overset{k_f}{\rightleftarrows}} C, \qquad \textbf{[S2]}$$

where A is the free particle, AA is the singly bound intermediate, and C is the doubly bound final state. At equilibrium, these can be rewritten in terms of the concentration of each species (square brackets denote concentration),

$$k_{on}[A]^2 = k_{off}[AA], \qquad \textbf{[S3]}$$

$$k_f[AA] = k_r[C]. \qquad \textbf{[S4]}$$

In addition, the total number of particles must be conserved, so this allows us to define a continuity equation,

$$C_0 = [A] + 2[AA] + 2[C]. \qquad \textbf{[S5]}$$

The only task left is to define the reaction rates. Prior work has revealed that the thermodynamics of single-particle binding is determined by the thermodynamics of a single DNA linkage (6); therefore, we hypothesize that single DNA thermodynamics will govern each hybridization/dehybridization event. In particular, we use the relationship,

$$K \equiv \frac{k_{on}}{k_{off}} = \exp\left(-\frac{\Delta G}{RT}\right), \qquad \textbf{[S6]}$$

where K is the equilibrium constant, ΔG is the Gibbs free energy of binding for a single DNA duplex, R is the universal gas constant, and T is temperature. It is interesting to note that the kinetics of the second reaction is also governed by individual DNA strands, the difference being their density. The reverse rate is given by:

$$k_r = 2k_{off}, \qquad \textbf{[S7]}$$

as there are two strands that could dehybridize to transition a doubly bound dimer to a singly bound dimer. The forward rate is determined by the availability of free linkers. Each particle has N linkers and can form bonds to n neighbors, i.e., $n = 12$ for an fcc lattice. In addition, the DNA sticky ends are restricted to a small volume V in the vicinity of the particle given by geometry and the polymer physics of DNA (6). Therefore, the forward rate is given by:

$$k_f = k_{on}\left[\frac{N}{V}\left(1 - \frac{2n}{N}\frac{[AA]}{C_0} - \frac{4n}{N}\frac{[C]}{C_0}\right)\right]^2, \qquad \textbf{[S8]}$$

where the rate reflects that binding is a second-order process and each linker strand that is bound cannot participate in further binding.

Now that the model is fully specified, an analytical solution can be derived. By combining Eqs. **S3** and **S5**, and using Eq. **S6** to define the rates in terms of thermodynamic quantities we find:

$$4[C]^2 + [C](8[AA] - 4C_0) + \left[(C_0 - 2[AA])^2 - \frac{[AA]}{K}\right] = 0. \qquad \textbf{[S9]}$$

In addition, we may combine Eq. **S4** with Eqs. **S7** and **S8** to find:

$$K[AA]\left[\frac{N}{V}\left(1 - \frac{2n}{N}\frac{[AA]}{C_0} - \frac{4n}{N}\frac{[C]}{C_0}\right)\right]^2 - 2[C] = 0. \qquad \textbf{[S10]}$$

Self-consistent solutions to Eqs. **S9** and **S10** may be found numerically to provide the thermodynamic configuration as a function of C_0, N, V, n, and K. Exploring the specific relationships between the thermodynamic configurations and design variables was done by adjusting these variables appropriately. Adjusting linker strength was taken into account by adjusting K as defined by Eq. **S6**. Adjusting linker number was taken into account by choosing N to match the number of equivalents added. Salt concentration was the most subtle design variable to take into account, and we hypothesized it would have two major effects: (*i*) ionic strength is logarithmically (7) related to the enthalpy of binding; and (*ii*) increased ionic strength increases the electrostatic screening thus increasing V. To estimate the change in V with respect to salt concentration, we consider the experimentally determined maximum loading of DNA on a particle as a function of salt concentration (8). Assuming that loading stops when the system reaches a consistent effective concentration, the maximum loading can be used to compute V as a function of salt concentration, which we find scales with concentration to the two-fifths power.

1. Hill HD, Mirkin CA (2006) The bio-barcode assay for the detection of protein and nucleic acid targets using DTT-induced ligand exchange. *Nat Protoc* 1(1):324–336.
2. Hurst SJ, Han MS, Lytton-Jean AKR, Mirkin CA (2007) Screening the sequence selectivity of DNA-binding molecules using a gold nanoparticle-based colorimetric approach. *Anal Chem* 79(18):7201–7205.
3. Jin R, Wu G, Li Z, Mirkin CA, Schatz GC (2003) What controls the melting properties of DNA-linked gold nanoparticle assemblies? *J Am Chem Soc* 125(6):1643–1654.
4. Cullity BD, Stock SR (2001) *Elements of X-Ray Diffraction* (Prentice Hall, Upper Saddle River, NJ), 3rd Ed.
5. Arnold BC, Beaver RJ (2000) The skew-Cauchy distribution. *Stat Probab Lett* 49(3): 285–290.
6. Macfarlane RJ, et al. (2010) Establishing the design rules for DNA-mediated programmable colloidal crystallization. *Angew Chem Int Ed Engl* 49(27):4589–4592.
7. Petruska J, Goodman MF (1995) Enthalpy-entropy compensation in DNA melting thermodynamics. *J Biol Chem* 270(2):746–750.
8. Hurst SJ, Lytton-Jean AKR, Mirkin CA (2006) Maximizing DNA loading on a range of gold nanoparticle sizes. *Anal Chem* 78(24):8313–8318.

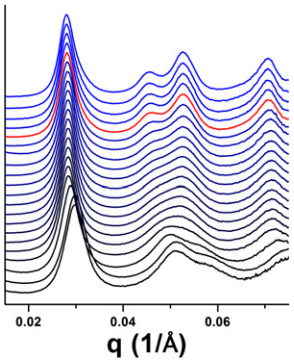

Fig. S1. Stacked plot of a single kinetics experiment where the *y* axis signifies the progression of time, starting from an initial disordered scan at room temperature (bottom trace). The red trace indicates the transition point described above, where there is a clear local minimum between the third- and fourth-order peaks.

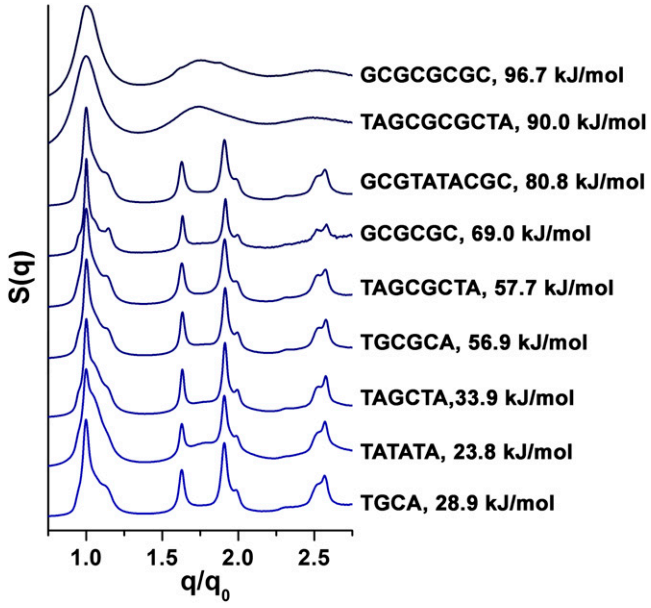

Fig. S2. Comparison of normalized SAXS patterns for assembly systems using sticky end sequences of different strengths [base sequence and calculated magnitudes of ΔG (5) adjacent to each trace] after being placed at their optimal annealing conditions for ~24 h. Most systems formed crystals of essentially identical quality and the two strongest sticky end sequences tested formed only disordered structures, indicating that there is an "upper limit"—sticky end interactions above this limit are too strong to enable reorganization on an appreciable time scale.

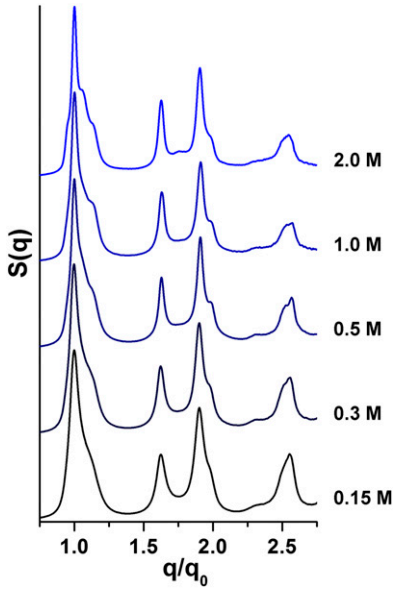

Fig. S3. Normalized SAXS patterns of systems at different salt concentrations (0.15 to 2.0 M NaCl) after overnight incubation at their respective optimal annealing conditions. All systems formed crystals of similar quality.

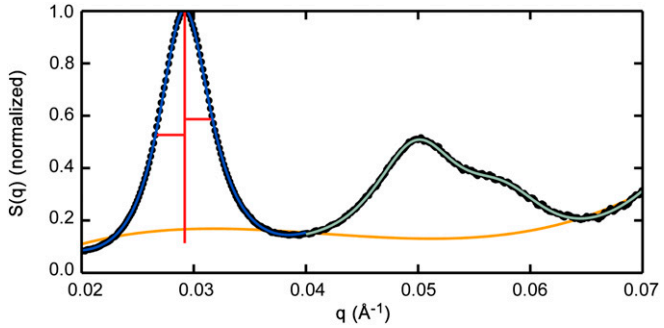

Fig. S4. Representative results from the fitting protocol. Normalized data are shown as black dots. Initial background fitting is shown as a smooth orange line. Fitting to the first two and second two peaks are shown as light blue and light green lines, respectively. The vertical and horizontal red lines signify the values used for a simple measurement of peak width.

Table S1. DNA sequences used to assemble nanoparticles

Strand type	Sequence	
Linker DNA	5′ TTG CTG AGT ATA ATT GTT – A - . . . . 3′	
AuNP-bound DNA	5′ AAC AAT TAT ACT CAG CAA - (nonbinding region) - SH 3′	
Self-complementary sticky ends	5′. . . .TGCA 3′	5′. . . .TGCGCA 3′
	5′. . . .GCGC 3′	5′. . . .GCGCGC 3′
	5′. . . .TATATA 3′	5′. . . .GCGTATACGC 3′
	5′. . . .TAGCTA 3′	5′. . . .TAGCGCGCTA 3′
	5′. . . .TAGCGCTA 3′	5′. . . .GCGCGCGC 3′

A single standard sequence was used for the thiol-modified strand bound to the nanoparticle surface; this sequence contained a 3′-propylthiol moiety, 12 ethylene glycol units (synthesized using spacer phosphoramidite 18 obtained from Glen Research and attached to the DNA strands with standard phosphoramidite chemistry), and an 18-base region complementary to the sequence at the 5′ end of the linker strands. All DNA linkers contained the same particle recognition sequence, followed by a single unpaired flexor base and a short sticky end sequence—the terminal sticky end at the 3′ end of the linker was varied as described in the main text.

Table S2. Average crystal domain sizes and melting temperatures for different systems tested including sticky end sequences, number of linker equivalents per particle, and solution salt concentration

Sticky end	T_m (°C)	Average domain size (nm)	ΔG_{se} (kJ/mol)	Linker equivalent	Salt concentration
TGCA	30.5	700	28.9		
TATATA	41.2	610	23.8		
TAGCTA	44.3	910	33.9		
TGCGCA	57.0	850	56.9		
TAGCGCTA	58.1	700	57.7		
GCGCGC	60.3	1250	69.0		
GCGTATACGC	59.4	740	80.8		
TAGCGCGCTA	62.6	200	90.0		
GCGCGCGC	63.4	240	97.1		
TAGCTA	39.1	310		20×	
TAGCTA	41.1	380		30×	
TAGCTA	40.7	670		40×	
TAGCTA	45.3	490		45×	
TAGCTA	44.3	560		60×	
TAGCTA	47.2	510		80×	
TAGCTA	48.5	390		100×	
TAGCTA	31.0	510			0.15 M
TAGCTA	40.0	580			0.30 M
TAGCTA	44.3	680			0.50 M
TAGCTA	50.5	660			1.0 M
TAGCTA	54.1	760			2.0 M

Domain sizes were calculated using the Scherrer formula and reflect the endpoint of crystal growth after 24 h of annealing at each sample's optimal annealing temperature.

Table S3. Analysis from fitting of the scattering data for different sticky end sequences

		First-order peak				Fourth-order peak			
Linker sequence (melting temperature)	Temperature (°C)	Time constant (s)	Error	Asymptote ($\times 10^{-3}$)	Error ($\times 10^{-3}$)	Time constant (s)	Error	Asymptote ($\times 10^{-3}$)	Error ($\times 10^{-3}$)
TGCA (30.5 °C)	22.0	207.9	14.2	3.92	0.016	332.9	77.1	8.86	0.40
	26.0	89.4	12.5	3.75	0.024	45.9	4.94	7.62	0.15
	30.0	54.6	9.74	3.54	0.042	43.6	10.6	6.12	0.30
	31.5	79.8	40.2	3.26	0.016	20.4	4.20	6.23	0.19
TAGCTA (44.3 °C)	41.0	165	47.0	3.97	0.062	1051	187	8.54	0.05
	42.5	64.8	11.2	3.96	0.019	348	35.4	7.52	0.29
	44.0	71.9	15.5	3.77	0.033	89.3	13.4	7.36	0.29
	45.5	45.7	8.92	3.46	0.050	40.1	9.16	5.90	0.41
	46.5	45.8	5.02	2.44	0.041	11.2	1.59	3.80	0.17
TGCGCA (57.0 °C)	55.5	182.9	35.2	3.47	0.070	280.6	26.3	6.37	0.28
	57.0	142.8	23.3	3.03	0.093	132.8	12.6	5.02	0.23
	58.0	97.4	14.4	2.92	0.068	110	17.2	4.56	0.37
	59.0	159.8	34.5	2.21	0.186	114.1	23.6	3.63	0.59
GCGCGC (60.3 °C)	62.0	762.3	231.8	1.69	0.627	131.2	11.6	4.61	0.23
	63.5	469.6	56.7	2.01	0.207	170.9	18.8	4.49	0.41
	65.0	105.7	15.7	2.49	0.118	50.8	7.16	4.69	0.21

For each sticky end sequence tested, the temperature at which the experiment was performed is listed. FWHM of scattering peaks were fit (see *SI Text, Data Analysis*) to a curve, then plotted as a function of annealing time. These data were then fit to a single exponential function, and the corresponding time constants and asymptote values for the first- and fourth-order peaks are listed here.

Table S4. Analysis from fitting of the scattering data for different linker equivalents added

		First-order peak				Fourth-order peak			
Linker equivalents (melting temperatures)	Temperature (°C)	Time constant (s)	Error	Asymptote ($\times10^{-3}$)	Error ($\times10^{-3}$)	Time constant (s)	Error	Asymptote ($\times10^{-3}$)	Error ($\times10^{-3}$)
45× (45.3 °C)	40.0	32.7	2.54	3.27	0.016	81.8	8.98	6.57	0.18
	42.0	28.9	3.75	3.08	0.033	34.0	4.43	5.91	0.15
	44.0	22.6	2.10	2.74	0.024	18.4	1.78	4.51	0.12
	45.5	14.9	2.05	2.54	0.034	11.1	0.84	3.69	0.10
60× (44.3 °C)	42.0	44.1	3.62	3.42	0.014	69.5	7.45	6.73	0.17
	44.0	49.3	8.05	3.16	0.033	16.2	3.30	6.16	0.15
	46.0	12.9	2.34	3.05	0.025	12.4	1.99	4.64	0.15
	47.5	46.8	7.36	2.73	0.061	32.6	5.38	3.42	0.31
80× (47.2 °C)	44.0	76.0	8.48	3.69	0.026	134.5	36.6	6.03	0.86
	45.5	54.1	5.58	3.46	0.024	49.6	6.99	6.37	0.21
	47.0	29.3	5.44	3.37	0.035	35.0	5.50	5.13	0.21
	48.5	209.9	65.3	2.13	0.305	26.7	4.20	4.08	0.20

For each linker density tested, the temperature at which the experiment was performed is listed with the corresponding time constant and asymptote values for the first- and fourth-order peaks (see *SI Text, Data Analysis* and Table S3 for description).

Table S5. Analysis from fitting of the scattering data for different salt concentrations

		First-order peak				Fourth-order peak			
Salt concentration (melting temperature)	Temperature (°C)	Time constant (s)	Error	Asymptote ($\times10^{-3}$)	Error ($\times10^{-3}$)	Time constant (s)	Error	Asymptote ($\times10^{-3}$)	Error ($\times10^{-3}$)
TAGCTA 0.15 M (31.0 °C)	29.5	203.8	21.6	3.95	0.0226	375.6	68.4	6.89	0.42
	31.0	83.4	10.7	3.87	0.0283	111.7	28.1	6.90	0.47
	32.5	44.7	6.52	3.62	0.0526	54.8	7.77	6.20	0.20
	34.0	28.8	4.93	3.49	0.0509	28.1	3.54	4.78	0.18
TAGCTA 0.3 M (40.0 °C)	36.5	166.6	29.8	3.62	0.0300	272.8	73.4	6.57	0.65
	38.0	60.6	15.7	3.77	0.0414	99.4	9.17	6.59	0.17
	40.0	38.2	3.77	3.69	0.0137	32.2	4.98	6.12	0.21
	41.5	141.9	28.1	2.91	0.0936	24.2	3.39	4.91	0.20
TAGCTA 0.5 M (44.3 °C)	42.0	44.1	3.62	3.42	0.0135	69.5	7.45	6.73	0.17
	44.0	49.3	8.05	3.16	0.0330	16.2	3.30	6.16	0.15
	46.0	12.9	2.34	3.05	0.0249	12.4	1.99	4.64	0.15
	47.5	46.8	7.36	2.73	0.0614	32.6	5.38	3.42	0.31
TAGCTA 1.0 M (50.5 °C)	44.0	116.8	18.2	3.63	0.0310	178.5	61.6	8.58	0.89
	46.0	81.7	9.30	3.26	0.0327	89.1	20.4	6.75	0.45
	48.0	47.0	7.44	2.98	0.0437	15.3	2.13	6.41	0.15
	50.0	15.2	2.37	2.86	0.0223	22.6	3.65	4.74	0.14
	51.0	19.2	3.49	2.67	0.0403	16.8	0.99	4.38	0.11

For each salt concentration tested, the temperature at which the experiment was performed is listed with the corresponding time constant and asymptote values for the first- and fourth-order peaks (see *SI Text, Data Analysis* and Table S3 for description).